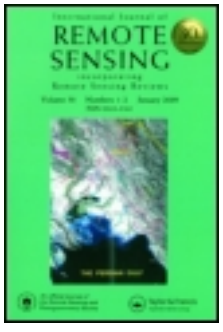

International Journal of Remote Sensing

Publication details, including instructions for authors and subscription information:
http://www.tandfonline.com/loi/tres20

Comparison between observed and synthetic 6.5 and 10.7 μm GOES-12 imagery of thunderstorms that occurred on 8 May 2003

Lewis D. Grasso [a], Manajit Sengupta [a] & Mark Demaria [b]

[a] Cooperative Institute for Research in the Atmosphere/Colorado State University, 1375 Campus Delivery, Fort Collins, Colorado, 80523-1375, USA

[b] NOAA/NESDIS/ORA/RAMMB, Fort Collins, Colorado, USA

Version of record first published: 23 Feb 2010

To cite this article: Lewis D. Grasso, Manajit Sengupta & Mark Demaria (2010): Comparison between observed and synthetic 6.5 and 10.7 μm GOES-12 imagery of thunderstorms that occurred on 8 May 2003, International Journal of Remote Sensing, 31:3, 647-663

To link to this article: http://dx.doi.org/10.1080/01431160902894483

International Journal of Remote Sensing
Vol. 31, No. 3, 10 February 2010, 647–663

Taylor & Francis
Taylor & Francis Group

Comparison between observed and synthetic 6.5 and 10.7 μm GOES-12 imagery of thunderstorms that occurred on 8 May 2003

LEWIS D. GRASSO*†, MANAJIT SENGUPTA† and MARK DEMARIA‡
†Cooperative Institute for Research in the Atmosphere/Colorado State University, 1375 Campus Delivery, Fort Collins, 80523–1375, Colorado, USA
‡NOAA/NESDIS/ORA/RAMMB, Fort Collins, Colorado, USA

(*Received 24 July 2008; in final form 6 February 2009*)

Over the past few years, a numerical system to produce synthetic satellite images has been developed at the Cooperative Institute for Research in the Atmosphere. This is being done to better understand imagery from current and future sensors. This system consists of a mesoscale model and an observational operator. Synthetic imagery of a boundary layer capped stratus cloud and an idealized thunderstorm have been produced by past investigators. In this publication, this system was applied to a thunderstorm event that occurred over the central plains of the USA on 8 May 2003. The main purpose of this study is to extend previous research by comparing observed and synthetic GOES-12 imagery of thunderstorms from an observed event. Synthetic 6.5 and 10.7 μm GOES-12 satellite imagery was produced and compared to actual 6.5 and 10.7 μm GOES-12 imagery from 8 May 2003. Multiple two-way interactive nested grids and two-moment microphysics were employed in this study. Various statistics were used to compare synthetic satellite imagery with observed satellite imagery. Results show that the synthetic imagery was reasonably similar to observed imagery. An approximate 2% cold bias, though, was evident in the synthetic imagery associated with the tops of the simulated thunderstorms. When the calculation of brightness temperatures was done a second time, the number of vertical levels was increased an order of magnitude: the 2% cold bias remained. This led to the conclusion that the bias was related to simulated thunderstorms that were more intense than observed thunderstorms and possibly cooler simulated tropopause temperatures.

1. Introduction

Recent efforts at the Cooperative Institute for Research in the Atmosphere (CIRA) have concentrated on the development of synthetic satellite imagery. Motivation for such a system is threefold: (1) to better understand and interpret currently available satellite imagery; (2) to prepare for next generation satellite systems—GOES-R and NPOESS, for example; and (3) to verify operational numerical weather prediction using synthetic satellite imagery.

Greenwald *et al*. (2002) reported on the development of an observational operator that was designed to create synthetic Geostationary Operational Environmental Satellite-9 (GOES-9) imagery. Synthetic imagery was created at 0.629, 3.92, 6.77, 10.72 and 12.01 μm for a scene containing a low level stratus cloud layer, composed

*Corresponding author. Email: grasso@cira.colostate.edu

International Journal of Remote Sensing
ISSN 0143-1161 print/ISSN 1366-5901 online
http://www.tandf.co.uk/journals
DOI: 10.1080/01431160902894483

entirely of liquid water, which occurred on 2 May 1996 over Texas and Oklahoma. The Regional Atmospheric Modeling System (RAMS) was used to simulate that event using one-moment microphysics for cloud water. A comparison was conducted between observed brightness temperatures of cloudy pixels with synthetic brightness temperatures of simulated cloudy pixels (see their figure 9). Results demonstrated good agreement between observed and synthetic imagery.

Grasso and Greenwald (2004) extended the above system (RAMS plus observational operator) to an idealized thunderstorm simulation. In particular, the observational operator was further developed to calculate optical properties of several additional hydrometeor species: pristine ice, snow, aggregates, graupel, hail and rain water. Although cloud liquid water was computed using one-moment microphysics (only hydrometeor mass mixing ratio is predicted), all other hydrometeor types were computed using two-moment microphysics (hydrometeor mass mixing ratio and number concentration are predicted). Synthetic GOES-9 10.7 μm imagery was created for the idealized thunderstorm. Two features of some observed thunderstorms were evident in the synthetic imagery: an enhanced-V along with a downwind warm region in the anvil (see figure 3 of Grasso and Greenwald, 2004).

Grasso *et al.* (2008) discussed the use of a numerical cloud model in conjunction with an observational operator for future satellites. In particular, synthetic GOES-R advanced baseline imagery (ABI) was produced for the 8 May 2003 thunderstorm event that took place over the central plains of the United States. In addition, they pointed out that synthetic imagery can be used for algorithm development. Such algorithms could be used for the detection of thin cirrus or fires, for example. Synthetic imagery may be useful in the understanding of data from not only US satellites, but also other international satellites such as, but not limited to, the European Meteosat Series, the Multi-functional Transport Satellite program in Japan, the Indian National Satellite System, and a new satellite planned to be launched in the next few years: the Communication, Ocean and Meteorological Satellite (Choi *et al.* 2007).

Other groups have also developed techniques to produce synthetic imagery from simulated output. Data from the European Center for Medium Range Weather Forecasts (ECMWF) were used to produce synthetic imagery for validation purposes (Morcrette 1991). Synthetic satellite imagery has also been used for numerical weather prediction verification by comparing synthetic imagery from a forecast model to observed imagery (Panegrossi *et al.* 1998, Kummerow *et al.* 2001). More recently, Chaboureau and Pinty (2006) used this technique to assess a parameterization scheme. Raymond and Aune (2003) have taken output from the Cooperative Institute for Meteorological Satellite Studies (CIMSS) Regional Assimilation System (CRAS) model to produce synthetic imagery of a water vapour band.

This study extends the above efforts by producing synthetic GOES-12 6.5 and 10.7 μm imagery of the 8 May 2003 thunderstorm event and comparing them to observed GOES-12 imagery. This is a first attempt at comparing synthetic GOES-12 imagery of numerically resolved thunderstorms from a case study with observed GOES-12 imagery. Further, vertical grid spacings at the level of the anvil in the Grasso and Greenwald (2004) study were 2000 m. In contrast, vertical grid spacings in this study were reduced to 500 m at anvil level. Along with cloud-free regions, a mixture of cloud types existed on that day. As a result, computation of optical properties of all seven hydrometeor types was required. Further, observed GOES-12 6.5 and 10.7 μm imagery at approximately 10-minute intervals was available for the comparison.

Thus the severe weather case provides a wide variety of brightness temperatures which vary rapidly with time. As a result, this case represents a challenging test for the synthetic data system. In addition, satellite images near 6.5 and 10.7 μm have been used to examine channel differencing over thunderstorms (Ackerman 1996, Tjemkes *et al*. 1997). Synthetic imagery in these bands can be useful for satellite algorithm development and understanding information contained in channel differencing.

This paper is divided into six sections. §2 contains a brief description of RAMS and the observational operator. A brief overview of the 8 May 2003 thunderstorm event is found in §3. Comparison of the observed and synthetic GOES-12 imagery is presented in §4. A discussion of the discrepancies between the simulation and observations is contained in §5 followed by the summary and conclusions in §6.

2. Computational methodology

2.1 *RAMS*

In order to achieve spatial and temporal variations of hydrometeor mean diameters in conjunction with two-way communication between nested grids, RAMS-4.3 was chosen as the mesoscale model to simulate the thunderstorm event. Additional details of RAMS are discussed in Grasso and Greenwald (2004). Because the present simulation was a case study, additional features of RAMS were used compared to Grasso and Greenwald (2004) and they are listed below.

- The Chen-Cotton radiation scheme (Chen and Cotton 1983) was used for both longwave and shortwave radiation along with longitudinal variations of short wave irradiance. Radiation tendencies were updated every 900 s.
- Surface fluxes were computed using the Land Ecosystem Atmospheric Feedback model, version 2 (LEAF2) (Walko *et al*. 2000).

A total of four grids were used in this simulation. Horizontal grid spacings were 50 km, 10 km, 2 km, and 400 m for grids 1 through 4, respectively. Although output from grid 4 was not used to create synthetic GOES-12 imagery, this grid was necessary to resolve convection. Grid 3 had horizontal grid spacings of 2 km; which is small enough to *represent* convection but is near the upper limit to *resolve* such features. Vertical grid spacings were stretched from 100 m near the surface to 500 m near 4.5 km. Vertical grid spacings were fixed at 500 m from 4.5 km to the top of the domain—approximately 24 km. As a result, all grids had 60 vertical levels. Grasso and Greenwald (2004) also employed a stretched vertical grid. One main difference was that the vertical grid spacings in their study attained values of 2 km near the top of the simulated thunderstorm. In order to improve the vertical resolution of upper tropospheric cloud layers, a maximum vertical grid spacing of 500 m was used for this study. Due to memory limitations, the use of smaller vertical grid spacings was impractical. Grid 1 had 90×66 points in the horizontal direction and covered most of the USA. Grid 2 had 192×162 points and covered most of the central plains. Grid 3 had 502×522 points in the horizontal direction and was slightly smaller than Grid 2. Grid 4 had 1027×852 points and covered most of eastern Kansas (see figure 2 in Grasso *et al*. 2008). These values were chosen so that synthetic imagery could be produced over a relatively large region.

All three outer grids were initialized from the National Center for Environmental Prediction (NCEP) NAM model (formerly Eta) analysis data at 1200 UTC 8 May 2003. From 1200 UTC 8 May 2003, all three grids were advanced to 1800 UTC. At

this time, grid 4 was spawned. This is about two hours prior to the development of simulated thunderstorms. In contrast to grids 1–3, grid 4 was initialized from grid 3. All grids were then advanced to 2355 UTC at which time the simulation was terminated. From 1800 UTC to 2355 UTC model output from grid 3 was saved. This output was then used as input to the observational operator.

2.2 *Observational operator*

Gaseous absorption was computed from the simulated pressure, temperature, and water vapour fields from RAMS. Ozone was included and was based on a standard profile. Values of the single scattering albedo and extinction of the seven hydrometeor types were computed and combined. Values of the asymmetry parameter were set to 0.9 since calculated values from anomalous diffraction theory exhibited little variation from this value. This information was used by a one-dimensional radiative transfer model to compute GOES-12 brightness temperatures at 6.5 and 10.7 μm. Additional details of the observational operator can be found in Greenwald *et al.* (2002). Further, a discussion of how optical properties of several different hydrometeors were combined is contained in Grasso and Greenwald (2004).

3. Case study

As described in the introduction, a thunderstorm event provides a challenge to creating synthetic satellite imagery. As part of the Virtual Institute for Satellite Integration Training (VISIT) (Mostek *et al.* 2004) training activities, data were collected for the 8 May 2003 thunderstorm event. As a result, observed GOES-12 imagery was available to facilitate the comparison with synthetic GOES-12 imagery.

Thunderstorm development over eastern Oklahoma and Kansas on 8 May 2003 was associated with a region of low pressure over western Nebraska. A warm front extended eastward along the Kansas Nebraska border. Thunderstorm development along the warm front began in the afternoon at 2000 UTC. A few hours later, additional thunderstorms developed over eastern Kansas along a dryline. The dryline extended southward from the warm front through eastern Kansas continuing into Oklahoma. During this time, a cold front moved south-eastward from northern Colorado and spread over most of north-west Kansas. Although no thunderstorms developed along the cold front, regions of blowing dust existed. As a consequence, a variety of severe weather occurred in the central plains (figure 1). Additional details of this case can be found in Grasso *et al.* (2008).

4. Comparison of synthetic and observed GOES-12 imagery

Synthetic imagery of thunderstorms, from grid 3, was compared to observed imagery of thunderstorms during the period when extensive anvils existed. As a result, synthetic data at 2300, 2310, 2320, 2330, 2340 and 2350 UTC on 8 May 2003 were compared to observed data at 2302, 2310, 2315, 2325, 2332 and 2345 UTC on 8 May 2003. An observed GOES-12 10.7 μm image at 2345 UTC (figure 2(*a*)) shows the region of thunderstorms over the central plains. The corresponding synthetic GOES-12 10.7 μm image at 2355 UTC from grid 3 is shown in figure 2(*b*). Recall that the horizontal grid spacing in grid 3 was 2 km and the horizontal footprint of GOES-12 imagery is near 4 km. As a result, the 2 km synthetic data were degraded using a four point average, to 4 km. Chevallier and Kelly (2002) used a similar procedure to match

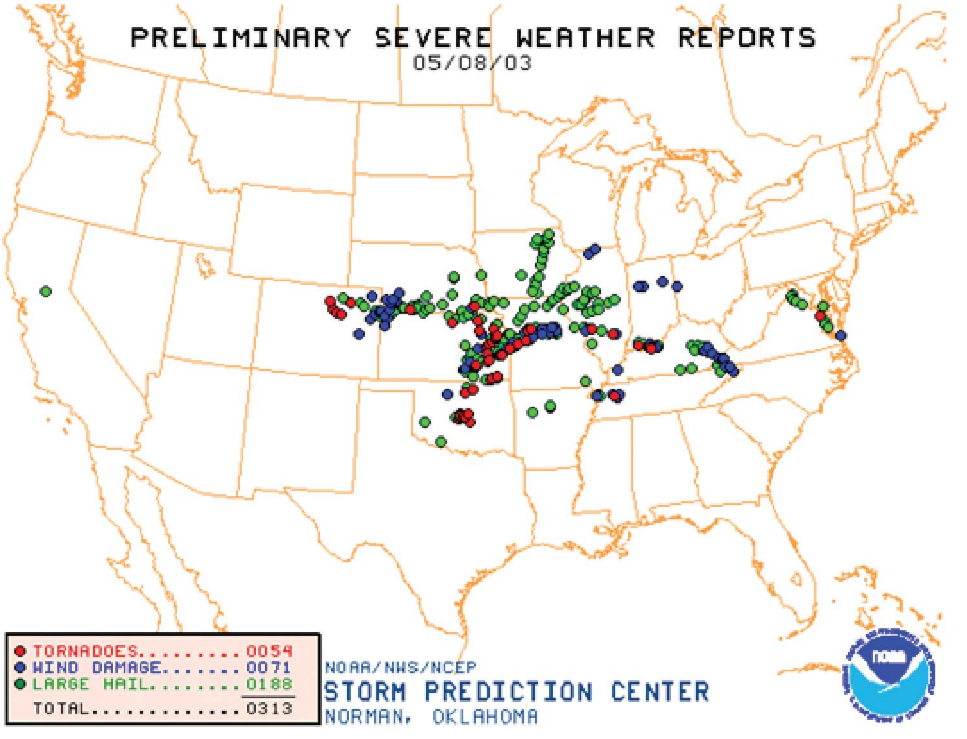

Figure 1. Storm reports, developed by the Storm Prediction Center, for 8 May 2003.

the footprint of synthetic satellite data to observed satellite data. Because the anvil canopies of thunderstorms are the features of interest, smaller geographical regions of the observed imagery (figure 2(*c*)) and synthetic imagery (figure 2(*d*)) were used for the comparison.

The comparison between synthetic cloudy pixels and observed cloudy pixels employed histograms. Histograms were also used by Chevallier *et al.* (2001) and Greenwald *et al.* (2002) as a method to compare synthetic and observed satellite data. In order to capture anvils of thunderstorms, brightness temperatures less than 233 K were used to screen the data at 6.5 and 10.7 μm. A value of 233 K also minimizes the impact of thin cirrus along anvil edges. Although vertical grid spacings were 500 m at anvil level, this value may be too large to resolve optically thin ice clouds at these two wavelengths.

For the scenes shown in figures 2(*c*) and 2(*d*), the corresponding histograms are displayed in figures 3(*a*) and 3(*b*). In general, both plots exhibit similar patterns. In addition, maxima in both plots are skewed towards colder temperatures. As indicated in the figures, cloud top brightness temperatures in figure 2(*c*) are warmer than those in figure 2(*d*). This is reflected in the histograms shown in figures 3(*a*) and 3(*b*). Further, observed anvil temperatures in figure 2(*c*) exhibit a larger range than those in figure 2(*d*). That is, a larger proportion of cloud top pixels in figure 2(*d*) exhibit a similar temperature. This explains why the region of maximum values in the histogram in figure 3(*a*) is wider and less peaked than those in figure 3(*b*).

A more comprehensive statistical analysis was performed with observed data from 2300 to 2345 UTC and synthetic data from 2300 to 2355 UTC. The resulting

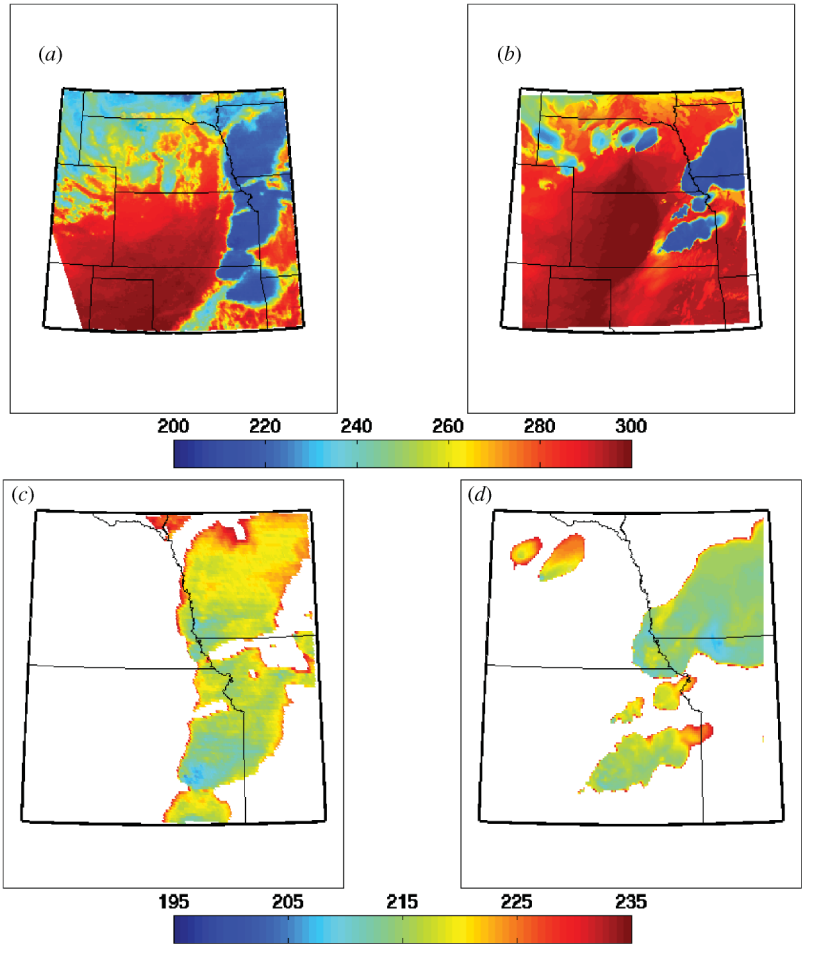

Figure 2. (*a*) GOES-12 10.7 μm image at 2345 UTC on 8 May 2003 and (*b*) synthetic GOES-12 10.7 μm image at 2355 UTC on 8 May 2003 for all of grid 3. Smaller regions were used to screen the observed and synthetic GOES-12 10.7 μm imagery. These regions are shown in (*c*) and (*d*), respectively. Brightness temperatures (K) are indicated by the colour bars.

histograms (figures 3(*c*) and 3(*d*)) also indicate features that were evident in figures 3(*a*) and 3(*b*). Observed brightness temperatures of the anvils were warmer and had a larger range of values about the maxima compared to those in the synthetic imagery. An additional statistic, the interquartile range, was used to quantify the dispersion of the brightness temperatures about the median value of the data shown in the histograms of figures 3(*c*) and 3(*d*). The interquartile range is denoted by the vertically dashed contours in both figures. At 10.7 μm, the interquartile range of the observed data is 2.9 K larger than the interquartile range of the synthetic data.

Observed and synthetic GOES-12 6.5 μm imagery were also compared. Observed imagery at 6.5 μm corresponding to the time and region of figure 2(*a*) is displayed in figure 4(*a*). Likewise, the synthetic 6.5 μm image corresponding to the time and region of figure 2(*b*) is displayed in figure 4(*b*). Histograms for the data shown in figures 4(*a*) and 4(*b*) are shown in figures 5(*a*) and 5(*b*), respectively. In both figures, the region of maximum values is skewed towards colder temperatures. By comparison, however,

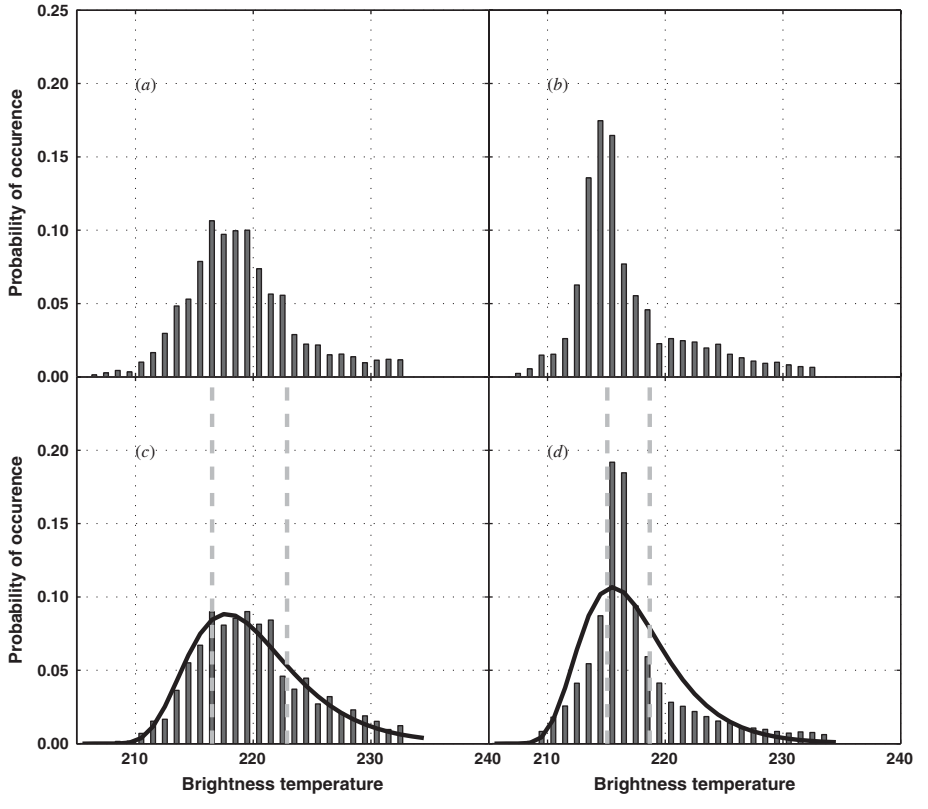

Figure 3. (*a*) Histogram for the observed image shown in figure 2(*c*). (*b*) Histogram for the synthetic image shown in figure 2(*d*). (*c*) Histogram and lognormal curve for observed imagery approximately every 10 minutes from 2300 to 2345 UTC. (*d*) Same as (*c*) but for synthetic data every five minutes from 2300 to 2355 UTC. The inter-quartile range is denoted by vertically dashed contours in (*c*) and (*d*).

the peak in the synthetic imagery existed at colder temperatures than the peak in the observed data. In addition, the region of the peak displayed in the observed histogram (figure 5(*a*)) is broader than the region of the peak in the histogram of the synthetic image (figure 5(*b*)). These two features were also evident in histograms produced using observed images from 2300 to 2345 UTC (figure 5(*c*)) and synthetic images from 2300 to 2355 UTC (figure 5(*d*)). At this wavelength, the interquartile range of the observed data was 1.9 K larger than that of the synthetic data.

Results displayed by the histograms from both 10.7 and 6.5 μm imagery exhibit similar features. Maximum values in the histograms for both wavelengths of the synthetic data existed at colder temperatures and had a smaller interquartile range of temperatures compared to the histograms of the observed data. Such a similarity between the histograms at 10.7 and 6.5 μm of the observed and synthetic imagery is somewhat expected. From the top of thunderstorm anvils to the top of the atmosphere, water vapour exists in relatively small amounts. One consequence is that additional absorption by water vapour of upwelling radiation at 6.5 μm is relatively small in that layer. Another way to demonstrate the similarities is to subtract brightness temperatures at 10.7 μm from those at 6.5 μm. This was done for the two observed images shown in figures 2(*c*) and 4(*c*), and the two synthetic images displayed

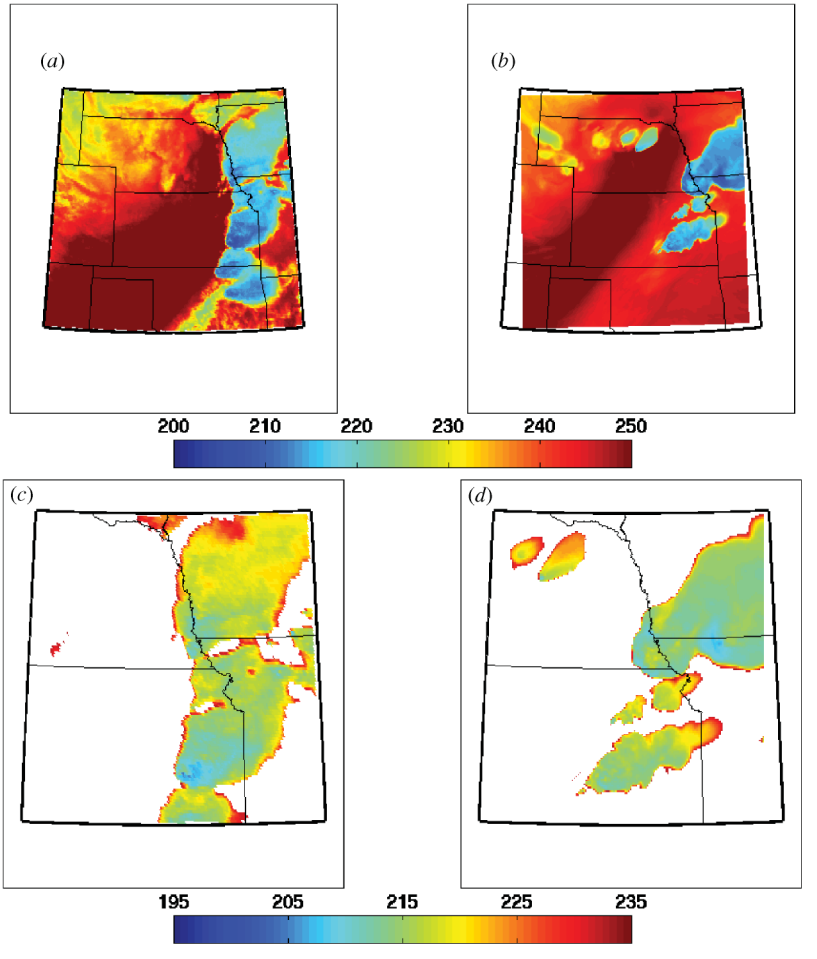

Figure 4. Same as figure 2 for 6.5 μm.

in figures 2(*d*) and 4(*d*). Observed differences are shown in figure 6(*a*) while differences for the two synthetic images are shown in figure 6(*b*). Results show a relatively small difference, approximately −1 K, between 6.5 and 10.7 μm for both observed and synthetic imagery. Furthermore, observed and synthetic differences are similar to each other. Channel differencing is an important tool for extracting additional information from satellite imagery. Further details about channel differencing the above two wavelengths can be found in Ackerman (1996) and Tjemkes *et al.* (1997).

Additional statistical methods were used to quantify the observed and synthetic data at 10.7 and 6.5 μm. A lognormal curve, based on the maximum likelihood estimate, was computed and added to the histograms in figures 3(*c*), 3(*d*), 5(*c*) and 5(*d*). Statistical data for the population making up the histograms and the lognormal curves are shown in table 1. Data in this table summarize the two main features of the observed and synthetic brightness temperatures: dispersion and average values.

Dispersion can be measured using the standard deviation of a dataset. As indicated by table 1, the standard deviations of the observed and synthetic datasets and the lognormal curves at a given wavelength are similar. Similar standard deviations

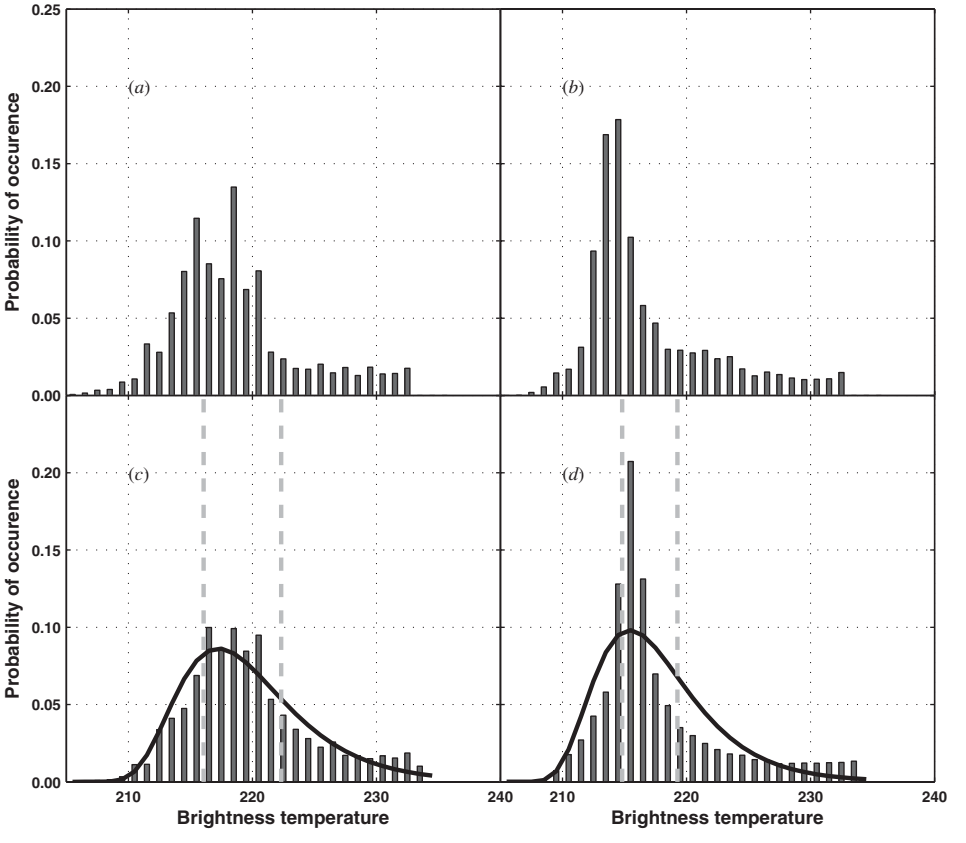

Figure 5. Same as figure 3 for 6.5 μm.

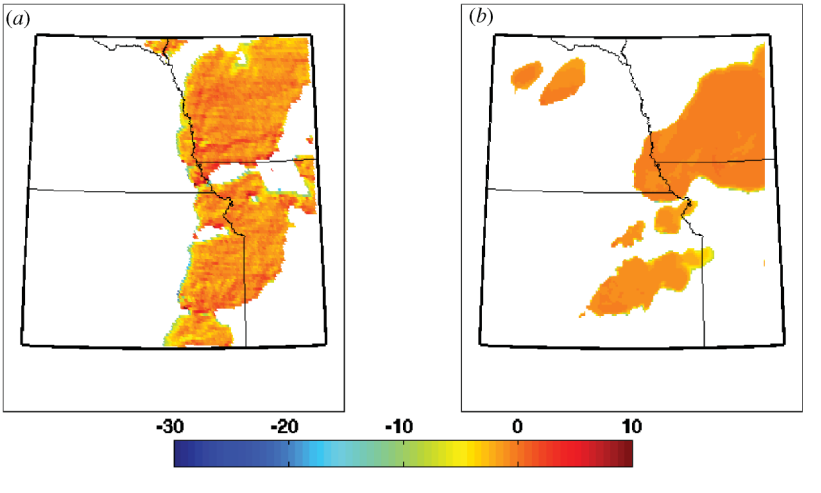

Figure 6. Brightness temperature difference (6.5–10.7 μm) for (*a*) observed imagery at 2345 UTC and (*b*) synthetic imagery at 2355 UTC.

Table 1. Population statistics of both observed brightness temperatures from 2300 to 2345 UTC and synthetic brightness temperatures from 2300 to 2355 UTC at 10.7 and 6.5 μm.

	Wavelength (10.7 μm)		Wavelength (6.5 μm)	
	Model	Observations	Model	Observations
Mean	216.5	220.1	216.8	219.2
Median	215.4	219.6	215.1	218.4
Standard deviation	4.50	4.80	5.14	5.13
Interquartile range	214.3–217.8	216.6–223.0	213.9–218.3	215.5–221.8
Maximum likelihood estimate of lognormal parameters				
Mean	2.466	2.657	2.478	2.632
95% confidence interval (mean)	2.465–2.467	2.654–2.660	2.476–2.479	2.629–2.635
Standard deviation	0.336	0.335	0.365	0.354
95% confidence interval (SD)	0.335–0.337	0.333–0.337	0.364–0.366	0.352–0.356

suggest similar dispersion between observed and synthetic brightness temperatures. This implication seems contradictory to the histograms themselves. The apparent contradiction can be resolved by considering a physical interpretation of the standard deviation. A component of the standard deviation is the distance from a data point to the mean value of the dataset. Consider the data points in figures 5(*c*) and 5(*d*) between 230 and 235 K. Because the population mean of the synthetic 6.5 μm data is 216.8 K, data points between 230 and 235 K have a greater distance compared to those in figure 5(*c*) where the population mean of the observed 6.5 μm dataset is 219.2 K. As a result, the standard deviation of the synthetic dataset is, coincidently, nearly identical to that of the observed data. The cause of the apparent contradiction arises due to the departure of both datasets from a normal distribution. This is the reason that the interquartile range was used, instead of the standard deviation, in the above discussion to describe dispersion of brightness temperatures.

Quantifying the average of the datasets was done by using the mean and median. Both of these values exhibited a cold bias for the synthetic data compared to observed data. Another way to show the cold bias is using percentiles during the one hour period. First the data were ordered from smallest to largest values of brightness temperatures. Starting from the lowest values of brightness temperatures, 5% of the data was combined to produce an average value. An average brightness temperature was then computed for each 5% interval until all the data were processed (figure 7). As seen in the figure, synthetic brightness temperatures in both channels were colder than observed values.

This simulation has served more than one purpose. One such purpose was to develop synthetic imagery for future satellites such as GOES-R (Grasso *et al*. 2008). This satellite will have a temporal sampling rate of 5 minutes. As a result, model output was specified at 5-minute intervals. This explains the mismatch of the observed and synthetic GOES-12 imagery in this paper. In order to examine the influence of this mismatch on the analysis, histograms, lognormal curves, and percentiles were repeated using 5-minute synthetic data along with the observed data during the same one hour time period. Results indicated that, in general, the statistics remained the same. In short, synthetic GOES-12 brightness temperatures had a smaller interquartile range and were about 2% lower than observed GOES-12 brightness temperatures.

Two possibilities exist that may explain the different dispersions between observed and synthetic brightness temperatures. First, weaker updrafts in observed

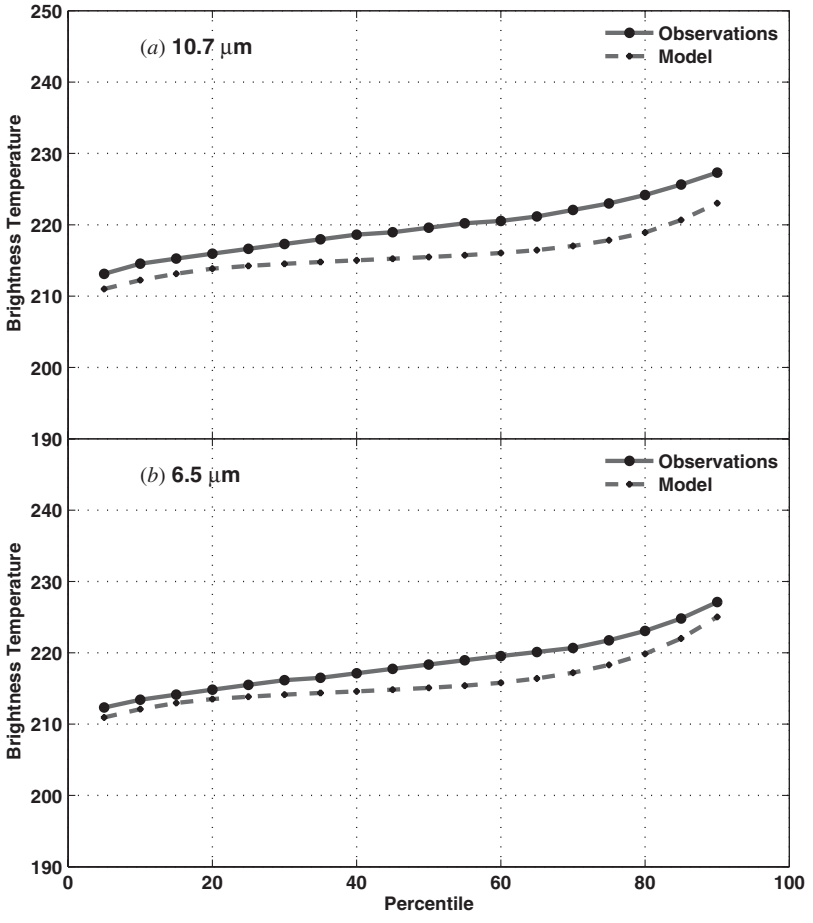

Figure 7. Percentile plots for a one hour period comparing observed and synthetic GOES-12 imagery at (*a*) 10.7 μm and (*b*) 6.5 μm.

thunderstorms would transport less condensate to the tropopause compared to stronger simulated thunderstorms. As a result of hydrometeor sedimentation and vertical shear, the observed anvil would be more susceptible to dissipation; consequently, observed brightness temperatures would tend to have more dispersion. Secondly, errors inherent in RAMS may have produced too much condensate in the simulated anvils. This could produce anvils that were less susceptible to dissipation. As a result, simulated brightness temperatures would tend to have less dispersion.

Four possibilities exists that may explain the cold bias in the synthetic imagery. First, differences may exist in the dataset used to initialize and nudge the simulation compared to observations. In particular, significant effort has been undertaken to improve initialization datasets via data assimilation techniques (Mesinger *et al*. 2006, Vukicevic *et al*. 2006). Secondly, simulated thunderstorms may have been more intense than observed thunderstorms. In particular, the equilibrium temperature of the simulated storms may have been lower than observed storms. Third, vertical grid spacings may have been too large at the top of the thunderstorms. That is, temperatures increased approximately 10 K in the top 1 km cloud layer of the simulated

thunderstorms. This increase was in response to the cold temperatures generated in overshooting domes. Further, with 500 m vertical grid spacing, the inversion associated with the tops of thunderstorms was *represented* by three model levels bounding two model layers. Layer temperatures were required by the observational operator; as a result, vertical averaging of temperatures from model levels to model layers was necessary. A cold bias could be created because of vertically averaging temperatures in a poorly *resolved* inversion located at the top of the thunderstorms. This possibility was tested by taking the model output at 2345 UTC and interpolating the entire domain to a new three dimensional domain in which vertical grid spacings were 50 m. As a result, the number of vertical grid points increased from 60 to nearly 500. Results from the observational operator showed that synthetic brightness temperatures did lower, but only in association with a relatively small area occupied near the overshooting dome. Therefore, reducing the vertical grid spacings was unable to explain the cold bias. This result suggests that the inversions near the top of the storm may only be associated with the overshooting dome as opposed to being a general characteristic of the anvil as a whole. No cold bias was indicated in the results of Greenwald *et al.* (2002) at 10.7 μm. The stratus cloud that was simulated existed near 1 km above the ground. Further, this cloud was nearly 400 m thick within an inversion of about 8 K per 1 km. Vertical grid spacings used in that study were 50 m from the surface to the top of the cloud layer. As a result of the 50 m grid intervals, the inversion within the cloud was fully *resolved*. Further, the departure of layer average temperatures from the level temperatures was significantly smaller in their case compared to the current study. Lastly, the cold bias may occur as a result of errors inherent to the observational operator and RAMS. As discussed by Greenwald *et al.* (2002), errors associated with radiative transfer calculations within the observational operator are approximately 1.5–2 K. One possible uncertainty concerning the parameterizations in RAMS deals with the microphysics. Simulated anvils contain three hydrometeor types away from the overshooting dome: pristine ice, snow, and aggregates. One method of mass removal from a simulated anvil is sedimentation of hydrometeors; another is parameterized mixing. At anvil level, static stability is relatively large and thus acts to dampen parameterized mixing processes. Sedimentation, therefore, would be the likely way to remove mass from an anvil and hence allow the anvil to appear warmer. Pristine ice self-collects to produce snow; snow self-collects to produce aggregates. Through further interactions between these three ice crystals, sedimentation of aggregates would remove ice mass from the anvil. Errors in hydrometeor collision, collection and sedimentation could artificially leave too much ice mass in the anvil. This could yield an anvil that appears cooler.

After the simulation was terminated, observed GOES-12 imagery began to show new thunderstorm development with colder brightness temperatures. This may suggest that the second possibility listed above may be the reason synthetic brightness temperatures of thunderstorm tops were colder than observations. That is, the simulated thunderstorms may have been more intense than observed storms during the period of analysis. Further, simulated tropopause temperatures may have been cooler than observations.

Histograms in figures 3 and 5 were generated using about 10-minute data over smaller regions of both the GOES-12 field of view (figures 2(*c*) and 4(*c*)) and grid 3 (figures 2(*d*) and 4(*d*)). Histograms were also generated using approximately 10-minute data for the one hour period beginning at 2300 UTC over all of grid 3 and the region of GOES-12 that was equivalent to the area covered by grid 3 (figure 8). In

general, histograms for observed 6.5 (figure 8(*a*)) and 10.7 μm (figure 8(*b*)) brightness temperatures exhibit a bi-modal distribution. This pattern is also evident in the histograms for synthetic 6.5 (figure 8(*c*)) and 10.7 μm (figure 8(*d*)) brightness temperatures. The bi-modal distribution was in response to three different source regions of radiant energy. Relatively cold cloud tops gave rise to the local maxima in the histogram from 210 to 230 K in not only observed and synthetic 6.5 μm imagery (figures 8(*a*) and 8(*c*)), but also observed and synthetic 10.7 μm imagery (figures 8(*b*) and 8(*d*)). Water vapour near the middle troposphere gave rise to the local maxima in the histogram at warmer temperatures ranging from 230 to 260 K in both the observed (figure 8(*a*)) and synthetic (figure 8(*c*)) 6.5 μm imagery. In contrast, low level clouds and the surface of the Earth gave rise to the local maxima in the histogram at warmer temperatures from about 270 to 300 K in both the observed (figure 8(*b*)) and synthetic (figure 8(*d*)) imagery at 10.7 μm.

Additional aspects of the observed and synthetic imagery for the entire domain of grid 3 are reflected in the histograms displayed in figure 8. In particular, the warmest brightness temperatures at 6.5 μm extend north-eastward from the Texas panhandle to eastern Nebraska in figures 4(*a*) and 4(*b*). In the observed image (figure 4(*a*)),

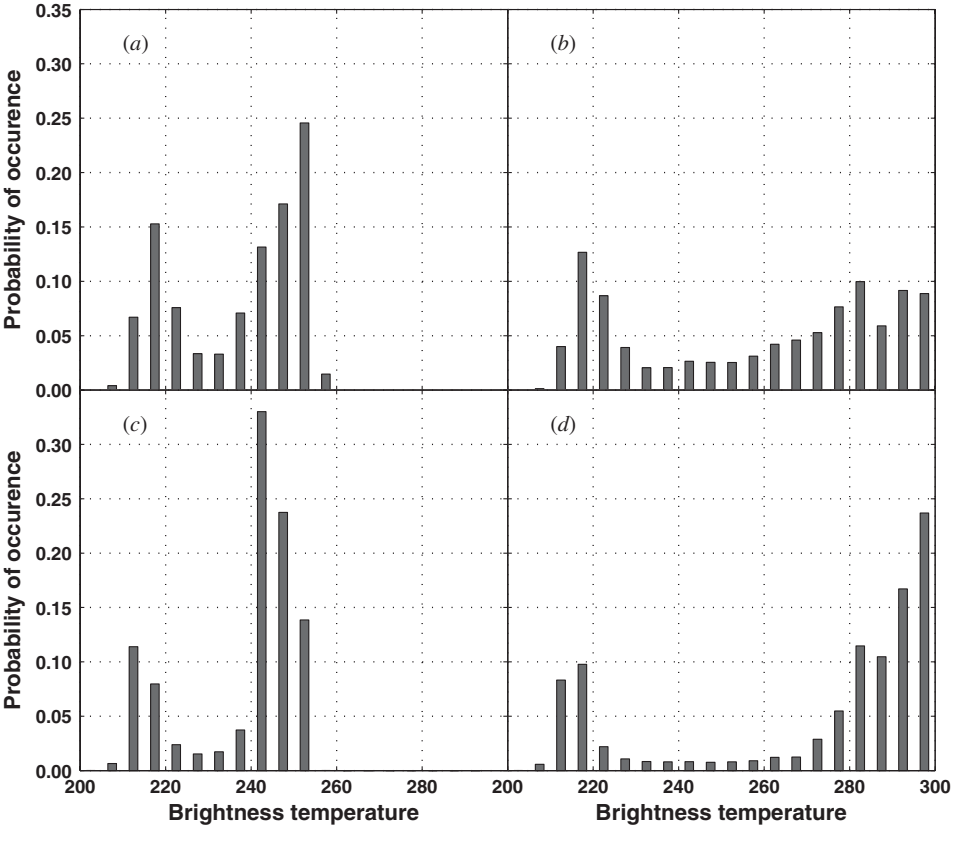

Figure 8. Histograms of (*a*) GOES-12 brightness temperatures at 6.5 μm, (*b*) GOES-12 brightness temperatures at 10.7 μm, both from 2300 to 2345 UTC; (*c*) synthetic brightness temperatures at 6.5 μm for grid 3, and (*d*) synthetic brightness temperatures at 10.7 μm for grid 3, both from 2300 to 2355 UTC.

however, this warm region occupied a larger geographical area, and consequently more pixels compared to the same region of the synthetic imagery (figure 4(*b*)). As a result, the histogram of the observed data (figure 8(*a*)) displays a larger value relative to the histogram of the synthetic data (figure 8(*c*)) at 250 K. Further, more observed thunderstorms existed compared to the simulated event. As a consequence, simulated data exhibited a larger percentage of brightness temperatures near 240 K and a smaller percentage of brightness temperatures near 215 K (figures 8(*a*) and 8(*c*)). Another aspect of the observed and synthetic data is evident in figures 2(*a*) and 2(*b*). Synthetic brightness temperatures at 10.7 μm over central Kansas are warmer compared to those in the observed data. This is also reflected in figures 8(*b*) and 8(*c*).

Differences between observed and synthetic imagery demonstrates the potential importance of synthetic satellite data for verification of forecast models. A comparison between observed and synthetic satellite data near 10.7 μm can be used to verify simulated surface temperatures. Recall, surface observations are not always available around the globe. Similarly, a comparison between observed and synthetic satellite data near 6.5 μm can be used to verify mid-tropospheric water vapour. In the future, synthetic satellite imagery from operational forecast models can be used in conjunction with data assimilation. One consequence may be an improved initial state and subsequent forecast.

5. Discussion

A subjective comparison between the observed and synthetic GOES-12 imagery at 10.7 μm (figures 2(*a*) and 2(*b*)) and 6.5 μm (figures 4(*a*) and 4(*b*)) suggest an endeavour to improve the simulation presented in this paper. Based on the authors' experience running RAMS, the timing and location of simulated deep tropospheric convection depends on several aspects of the numerical model. Some of these aspects are (1) the data used to initialize and laterally nudge the domain, (2) the choice of horizontal and vertical grid spacings, and (3) soil moisture.

Several choices of regional and global datasets exist that can be used to initialize and laterally nudge a numerical domain. Experience has shown that different datasets may yield different solutions at a given time in a simulation. This is especially true when running a simulation to capture convective initiation. In addition, differences in simulated convective activity may also depend on the start time of a simulation. As an example, on 4 April 2007 a line of thunderstorms developed over central and eastern portions of the USA during the afternoon. When this simulation was attempted, RAMS was started at 1200 UTC 4 April 2007. Similar to the case in this paper, some discrepancies were evident in the results. Because some convection existed at initialization time, the model was started at an earlier time. The question then became, how much earlier? Since results do depend on the initial state, changing the initialization time yields changes in the solution. This is why so much effort has been devoted to data assimilation techniques, particularly in cloudy atmospheres (Vukicevic *et al.* 2006). Data assimilation in cloudy atmospheres offers the potential to improve an initial state that contains clouds. Instead of initializing a model at a time with no convection, data assimilation would allow a model to be initialized at a time with convection. Furthermore, the existence of convection would be used by an assimilation system to improve an initial state. One consequence would be an improved simulation. In the case presented herein, data assimilation may yield weaker simulated convection and thus reduce the cold bias evident in the synthetic imagery. In addition,

convection exists on a scale that is smaller than the scale of the datasets that can be used for initialization purposes.

Horizontal and vertical grid spacings are also an important aspect of simulating deep tropospheric convection. Attempting to start a simulation at an earlier time, as in the above example, may require a domain to be expanded in the horizontal direction to capture a moving feature. Due to limitations of computer ram memory, expanding a domain may prevent smaller horizontal grid spacing from being established. This may set up the following scenario: on one hand, expanding a domain may be desirable to capture a moving feature; on the other hand, reducing horizontal grid spacings may be desirable to allow the model to resolve a feature of interest, convection for example. Limitations of computer memory may prevent both grid expansion and an increase in the number of grid points as a result of smaller grid spacings. Convective initiation may, at times, require horizontal grid spacings near or smaller than 1000 m. For the simulation in this paper, horizontal grid spacings of 400 m were required to allow additional convection to form. As figures 2 and 4 demonstrate, however, discrepancies still exists with regional coverage of convection. Relatively small grid spacing may be necessary to resolve boundary layer circulations on the scale of convection. Some of these circulations are driven by horizontal gradients of soil moisture.

Past studies have shown that convective initiation along a dryline can be dependent on horizontal variations of soil moisture (Ziegler *et al*. 1995, Shaw *et al*. 1997, Grasso 2000). Heterogeneous soil moisture can force stronger boundary layer circulations compared to those with a more homogeneous soil moisture profile. As a result, horizontal convergence and the resulting convective initiation become dependent on soil moisture patterns. Resolving such circulations, however, is dependent on the choice of horizontal and vertical grid spacings. As discussed above, grid spacings may be restricted by available computer memory.

For the case presented in this paper, first attempts of a simulation were conducted on a 32-bit computer. As a consequence of the issues contained in the above discussion, the simulation was moved onto a 64-bit computer in an attempt to improve the simulation. Different initialization times were used, different size grids were also used, and different amplitudes of soil moisture values were used while preserving the horizontal variability. Improving a simulation can be a challenge. Understanding processes leading to convective initiation remains an open question.

6. Summary and conclusions

Developing synthetic GOES imagery has been a continuing effort at CIRA over the past few years. Synthetic GOES-9 imagery of an observed stratus cloud layer was generated with RAMS and the newly developed observational operator. These models were then used to develop synthetic GOES-9 imagery of an idealized thunderstorm; followed by the generation of synthetic GOES-R ABI imagery. This study extends previous work by producing synthetic GOES-12 6.5 and 10.7 μm imagery of a thunderstorm event over the central plains of the USA on 8 May 2003.

Approximately 10-minute observed GOES-12 satellite data were compared with 10- and 5-minute synthetic GOES-12 data over a one hour period. Histograms, lognormal curves, and percentile plots were used to compare brightness temperatures for cloudy pixels associated with synthetic and observed thunderstorms. Statistical results suggest that the synthetic imagery compares favourably with the observed imagery. Further, results also demonstrated an approximate 2% cold bias associated

with synthetic imagery at 6.5 and 10.7 μm. The cold bias may be a result of more intense simulated thunderstorms and cooler simulated tropopause temperatures.

Future work will focus on the 6.5 and 10.7 μm brightness temperature difference associated with thunderstorm tops. Observations show that, at times, brightness temperatures near 6.5 μm are larger than those near 10.7 μm. The numerical system presented in this paper will be used to help explain the observed channel differences.

Acknowledgements

This material is based on work supported by the National Oceanic and Atmospheric Administration under Grant No. NA17RJ1228. Further, thanks are extended to Drs Stephen Tjemkes, Martin Setvak, Tim Schmit and Robert Aune for their helpful comments to improve this manuscript. The views, opinions, and findings in this report are those of the authors, and should not be construed as an official NOAA and or US Government position, policy, or decision.

References

Ackerman, S., 1996, Global satellite observations of negative brightness temperature differences between 11 and 6.7 μm. *Journal of Atmospheric Science*, **53**, pp. 2803–2812.

Chaboureau J.-P. and Pinty, J.-P., 2006, Evaluation of a cirrus parameterization with Metoesat Second Generation. *Geophysical Research Letters*, **33**, pp. 1–4.

Chen, C. and Cotton, W.R., 1983, A one-dimensional simulation of the stratocumulus-capped mixed layer. *Boundary-Layer Meteorology*, **25**, pp. 289–321.

Chevallier, F. and Kelly, G., 2002, Model clouds as seen from space: Comparison with geostationary imagery in the 11-μm window channel. *Monthly Weather Review*, **130**, pp. 712–722.

Chevallier, F., Bauer, P., Kelly, G., Jakob, C. and McNally, T., 2001, Model clouds over oceans as seen from space: Comparison with HIRS/2 and MSU radiances. *Journal of Climate*, **14**, pp. 4216–4229.

Choi, Y.-S., Ho, C.-H., Ahn, M.-H. and Kim, Y.-M., 2007, An exploratory study of cloud remote sensing capabilities of the Communication, Ocean and Meteorological Satellite (COMS) imagery. *International Journal of Remote Sensing*, **28**, pp. 4715–4732.

Grasso, L.D., 2000, A numerical simulation of dryline sensitivity to soil moisture. *Monthly Weather Review*, **128**, pp. 2816–2834.

Grasso, L.D. and Greenwald, T., 2004, Analysis of 10.7 μm brightness temperatures of a simulated thunderstorm with two-moment microphysics. *Monthly Weather Review*, **132**, pp. 815–825.

Grasso, L.D., Sengupta, M., Dostalek, J.F., Brummer, R. and DeMaria, M., 2008, Synthetic satellite imagery for current and future environmental satellites. *International Journal of Remote Sensing*, **29**, pp. 4373–4384.

Greenwald, T.J., Hertenstein, R. and Vukicevic, T., 2002, An all-weather observational operator for radiance data assimilation with moesoscale forecast models. *Monthly Weather Review*, **130**, pp. 1882–1897.

Kummerow C., Hong, Y., Olson, W.S., Yang, S., Adler, R.F., McCollum, J., Ferraro, R., Petty, G., Shin, D.-B. and Wilheit, T.T., 2001, The evolution of the Goddard Profiling Algorithm (GPROF) for rainfall estimation from passive microwave sensors. *Journal of Applied Meteorology*, **40**, pp. 1801–1820.

Mesinger, F., DiMego, G., Kalnay, E., Mitchell, K., Shafran, P.C., Ebisuzaki, W., Jovic, D., Woolen, J., Rogers, E., Berbery, E.H., Ek, M.B., Fan, Y., GruhPaine, R., Higgins, W., Li, H., Lin, Y., Manikin, G., Parrish, D. and Shi, W., 2006, North American regional reanalysis. *Bulletin of the American Meteorological Society*, **87**, pp. 343–360.

Morcrette J.-J., 1991, Evaluation of model-generated cloudiness: Satellite-observed and model-generated diurnal variability of brightness temperatures. *Monthly Weather Review*, **119**, pp. 1205–1224.

Mostek, A., Weaver, J., Bikos, D., Lindsey, D., Zajac, B., Bachmeier, S., Whittaker, T., Motta, B., Grant, B., LaDue, J. and Ferree, J., 2004, VISIT: Bringing training to weather service forecasters using a new distance leaning tool. *Bulletin of the American Meteorological Society*, **85**, pp. 823–829.

Panegrossi, G., Dietrich, S., Marzano, F.S., Mugnai, A., Smith, E.A., Xiang, X., Tripoli, G.J., Wang, P.K. and Poiares Baptista, J.P.V., 1998, Use of cloud model microphysics for passive microwave-based precipitation retrieval: Significance of consistency between model and measurement manifolds. *Journal of Atmospheric Science*, **55**, pp. 1644–1673.

Raymond, W.H. and Aune, R.M., 2003, Conservations of moisture in a hybrid Kuo-type cumulus parameterization. *Monthly Weather Review*, **131**, pp. 771–779.

Shaw, B.L., Pielke, R.A. and Ziegler, C.L., 1997, The effect of soil moisture heterogeneity on a Great Plains dry line: A numerical study. *Monthly Weather Review*, **125**, pp. 1489–1506.

Tjemkes, S.A., van de Berg, L. and Schmetz, J., 1997, Warm water vapour pixels over high clouds as observed by METEOSAT. *Contributions to Atmospheric Physics*, **70**, pp. 15–21.

Vukicevic, T., Sengupta, M., Jones, A.S. and Vonder Haar, T., 2006, Cloud resolving satellite data assimilation: information content of IR window observations and uncertainties in estimation. *Journal of Atmospheric Science*, **63**, pp. 901–919.

Walko, R.L., Band, L.E., Baron, J., Kittel, T.G.F., Lammers, R., Lee, T.J., Ojima, D., Pielke, R.A., Taylor, C., Tague, C., Tremback, C.J. and Vidale, P.L., 2000, Coupled atmosphere-biophysics-hydrology models for environmental modeling. *Journal of Applied Meteorology*, **39**, pp. 931–944.

Ziegler, C.L., Martin, W.J. Pielke, R.A. and Walko, R.L., 1995, A modeling study of a dryline. *Journal of Atmospheric Science*, **52**, pp. 263–285.